



HAL
open science

GaAs-Based Near-Field Thermophotonic Devices: Approaching The Idealized Case With One-Dimensional PN Junctions

Julien Legendre, Pierre-Olivier Chapuis

► **To cite this version:**

Julien Legendre, Pierre-Olivier Chapuis. GaAs-Based Near-Field Thermophotonic Devices: Approaching The Idealized Case With One-Dimensional PN Junctions. *Solar Energy Materials and Solar Cells*, 2022, 238, pp.111594. 10.1016/j.solmat.2022.111594 . hal-03294468v3

HAL Id: hal-03294468

<https://hal.science/hal-03294468v3>

Submitted on 9 Mar 2022

HAL is a multi-disciplinary open access archive for the deposit and dissemination of scientific research documents, whether they are published or not. The documents may come from teaching and research institutions in France or abroad, or from public or private research centers.

L'archive ouverte pluridisciplinaire **HAL**, est destinée au dépôt et à la diffusion de documents scientifiques de niveau recherche, publiés ou non, émanant des établissements d'enseignement et de recherche français ou étrangers, des laboratoires publics ou privés.

GaAs-Based Near-Field Thermophotonic Devices: Approaching The Idealized Case With One-Dimensional PN Junctions

Julien Legendre^{a,*}, Pierre-Olivier Chapuis^a

^aUniv Lyon, CNRS, INSA-Lyon, Université Claude Bernard Lyon 1, CETHIL UMR5008, F-69621, Villeurbanne, France

ARTICLE INFO

Keywords:

Near-field radiative heat transfer
Thermophotonics
Light-emitting diodes
Photovoltaics
GaAs

ABSTRACT

Thermophotonics (TPX) is a technology close to thermophotovoltaics (TPV), where a heated light-emitting diode (LED) is used as the active thermal emitter of the system. It allows to tune the heat flux, by means of electroluminescence, to a spectral range matching better the gap of a photovoltaic cell. The concept is extended to near-field thermophotonics (NF-TPX), where enhanced energy conversion is due to both electric control and wave tunneling. We perform a thorough numerical analysis of a GaAs-based NF-TPX device, by coupling a near-field radiative heat transfer solver based on fluctuational electrodynamics with an algorithm based on a simplified version of the drift-diffusion equations in 1D. This allows for the investigation of the emission and absorption profiles in the LED and the photovoltaic (PV) cell, and for the scrutiny of the impact of key parameters. We also demonstrate that the performance obtained with this algorithm can approach idealized cases for improved devices. For the considered simplified architecture and 300 K temperature difference, we find a power density output of 1 W.cm^{-2} , underlining the potential for waste heat harvesting close to ambient temperature.

1. Introduction

The necessity of a change in our relation with energy needs no longer to be proven. This change has to happen on several important topics: the generation of clean energy, the reduction of consumption of machines and buildings, and the recuperation of energy losses. On this last subject, recent solid-state heat engines avoid notably (potentially polluting) refrigerants and moving parts (thus vibrations). Thanks to these benefits, solid-state heat engines can be interesting candidates for both terrestrial and spatial applications.

Several of these engines have seen good recent development in the last 20 years thanks to dynamic research [1, 2]: we can cite thermoelectric devices [3, 4], thermophotovoltaic (TPV) devices [5], thermionic devices [6, 7] or hot-carrier cells [8, 9]. In the TPV field, if a large fraction of the research focuses on the development of improved emitters [10] or cell rear-face reflectors [11], advanced concepts are also under development [12], including hybridization with thermionic devices [13, 14], near-field (NF) enhancement [15–17] and thermophotonics (TPX) [18, 19]. In this work, we aim to study the combination of these last two concepts through the numerical analysis of a near-field thermophotonic (NF-TPX) device [20].

In a near-field thermophotovoltaic (NF-TPV) device, by decreasing the gap distance between the emitter and the photovoltaic (PV) cell to the order of hundreds of nanometers or below, evanescent waves start to participate to the heat transfer along with propagative modes [21]. Heat transferred to the PV cell can then be increased by a factor 10 to even 100 for small gap distances [17], exceeding therefore the blackbody limit and increasing by a similar order of magnitude the electrical power produced by the PV cell. However,

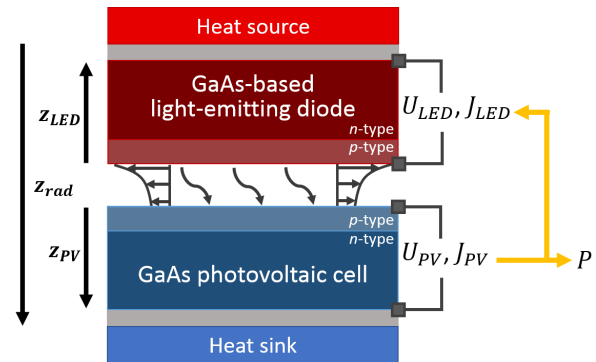


Figure 1: Schematic of a GaAs near-field thermophotonic device. The LED is maintained at 600 K, while the PV cell is kept at 300 K. In the nanogap, propagative and evanescent modes participate to the radiative heat transfer. Absorption of the radiation by the photovoltaic cell allows for the production of electrical power, a fraction of which is redirected towards the light-emitting diode for enhancement of the radiative heat transfer by electroluminescence. Ideal mirrors (in grey) allow for the confinement of photons inside the device.

the emitter cannot be controlled dynamically. The practical capabilities of such device have already been demonstrated [22–27].

Thermophotonic devices rely on the recent development of light-emitting diodes (LED). Thanks to the electroluminescent effect, the emission spectrum of the LED can be tuned by the application of a voltage, and can also exceed the blackbody limit. If most of this development was directed towards lighting applications, recent research has pointed out the interest of LEDs for thermodynamic applications as an electroluminescent refrigerator/heat pump [28–30] or as a key part of a TPX device. In the latter, the LED is placed in front of a PV cell and is heated above ambient temperature

*Corresponding author

✉ julien.legendre@insa-lyon.fr (J. Legendre)

ORCID(s): 0000-0001-7316-1954 (J. Legendre)

(in a heat engine configuration). Thanks to the electroluminescence effect, the radiative power transferred to the PV cell can be increased by order of magnitudes compared to the TPV case [18]. However, the LED is consuming electrical power: a TPX device can therefore produce electrical power only when made of high-efficiency LED and PV cell, this last argument being the reason of the recent interest in the device. Indeed, with the maturation of the LED technology, the achievable efficiency has increased largely in the last decades. Among the well-known semiconductors regularly used for PV and TPV applications, gallium arsenide (GaAs) junctions has reached extremely high internal and external quantum efficiencies (above 99% [31]), making it an ideal candidate for TPX application as underlined by the Aalto group [30], even with a larger bandgap energy than what is usually used for TPV (i.e. closer to visible than to mid-infrared).

By combining near-field effects with electroluminescent enhancement in a NF-TPX device, the radiative heat transfer increase is coupled and permits a dramatic increase of the electrical power output. Due to the limited temperatures current LEDs can withstand (600 to 700 K, see the review on high-temperature pn junctions in [32]), this kind of device is ideal for low-grade heat recovery application. This could allow for a photonic device to be performant in a range where standard TPV is barely used [5, 10, 11] because of its poor efficiency [1], being then competitive against thermoelectrics, a technology commonly used in this range of temperature [4].

In the first article on NF-TPX written by Zhao *et al.* [20], a 1D near-field radiative heat transfer (NF-RHT) model was coupled with a 0D detailed balance (DB) model for the computation of the currents. We propose here to analyze the performance of a GaAs NF-TPX device, by coupling a similar NF-RHT code with an improved charge carrier behaviour model relying on the solution of the simplified drift-diffusion (SDD) equations in 1D, often used in standard PV studies [33, 34].

2. Modelling

The NF-TPX device considered is shown in Figure 1. The PV cell is a GaAs pn junction, while the LED is made of a GaAs-based alloy (this matter is discussed in the next paragraph). The p- and n-regions are respectively the front and back layers of the two junctions. The LED is heated at 600 K, which allows for large radiative heat transfer while keeping the quantum efficiency high [35, 36]. The PV cell is kept at ambient temperature (300 K). On the back surface of the junctions, two perfect mirrors (i.e., with a dielectric function with an infinitely large real part and a null imaginary part) allows for the confinement of the photons inside the device. The main device parameters are shown in Table 1. On the right of Figure 1 are provided the main electrical parameters, where U is the voltage and J the current density. P represents the electrical power density

Table 1

Device parameters. The first value given is related to the LED, the second one to the PV cell. Opt. 1 refers to the optimized values obtained with surface recombinations, Opt. 2 to those obtained without surface recombinations (see Section 4.3).

Parameter	Unit	Symbol	Ref.	Opt. 1	Opt. 2
Temperature	K	T	600 300		
P-region doping	cm^{-3}	N_a	10^{20} 10^{20}		
N-region doping	cm^{-3}	N_d	10^{18} 10^{18}		
Gap distance	nm	d	10		
Mirror thickness	nm	t_m	10		
P-region thickness	nm	t_p	400	10	10
N-region thickness	nm	t_n	400	10	10
			10^4	10^4	500
			10^4	10^4	10^3

produced by the device.

The modelling process can be divided into two main steps:

- calculation of the near-field radiative heat transfer (including both below and above-bandgap photons, see Section 2.1)
- calculation of the I-V characteristic through the modelling of the charge carrier behaviour (see Section 2.2)

The different modelling parameters used in this work can be found in Table 2. By taking into account the variation of GaAs bandgap with temperature [37], the bandgap of a GaAs LED goes down to 1.28 eV, which has a significant impact on performances due to bandgap mismatch with the PV cell ($E_g^{300\text{K}} = 1.42$ eV). Instead of pure GaAs, the LED is therefore made of a GaAs-based alloy, which displays a bandgap of 1.42 eV at 600 K. In addition, optical properties of such alloys are very close to those of GaAs at 300 K (precisely because the bandgaps are matched). This allows us to model the performance of a GaAs-based LED using well-known GaAs optical properties at 300 K and electrical properties at 600 K. In this paper, we indistinctly refer to the device as 'GaAs NF-TPX' or 'GaAs-based NF-TPX', the LED being always made of GaAs-based alloys to keep its bandgap matched with that of the PV cell.

2.1. Near-field radiative heat transfer

The near-field radiative heat transfer between the LED and the PV cell is simulated using the Fluctuational Electrodynamics theory developed by Rytov [44], which allows for an accurate description of both propagative, frustrated and surface modes, the two latter being evanescent modes that are not described by the macroscopic framework. The random movement of charges at any point, characterized by the Fluctuation-Dissipation Theorem, can be linked to the electromagnetic wave perceived at any other point through Green tensors. Then, the radiated power is simply obtained as the mean value of the Poynting vector. By using Francoeur's formalism [45], the spectral photon flux density γ_ω ,

Table 2
 Modelling parameters.

Parameter	Unit	Symbol	Value	Reference
Bandgap energy	eV	E_g	1.42	[38]
Dielectric function	-	ϵ		
Interband [37]				
Drude-Lorentz [39, 40]				
Static rel. permittivity	-	ϵ_s	12.9	[41]
Electron rel. eff. mass	-	m_e^*	0.063	[41]
Hole rel. eff. mass	-	m_h^*	0.53	[41]
Electron mobility	$\text{cm}^2 \cdot \text{V}^{-1} \cdot \text{s}^{-1}$	μ_e		[42]
Hole mobility	$\text{cm}^2 \cdot \text{V}^{-1} \cdot \text{s}^{-1}$	μ_h		[42]
SRH recomb. coeff.	s^{-1}	A	3×10^5	[29]
Auger recomb. coeff.	$\text{cm}^6 \cdot \text{s}^{-1}$	C	10^{-30}	[29]
Surf. recomb. coeff.	$\text{m} \cdot \text{s}^{-1}$	S_n	5×10^2	[43]

which is related to the spectral heat flux density q_ω as $q_\omega = \hbar\omega\gamma_\omega$, emitted at a layer s and received at a position z_l in layer l can be expressed as

$$\gamma_{\omega,sl}(z_l) = (n_s^0 - n_l^0) \mathcal{T}_{sl}(z_l) = \gamma_{\omega,sl}^{in}(z_l) - \gamma_{\omega,sl}^{out}(z_l). \quad (1)$$

In this expression, n^0 is the modified Bose-Einstein distribution, which is tuned by means of electroluminescence through the value of the electrochemical potential μ (defined as the difference between the electron and hole quasi Fermi levels $\mu = E_{Fn} - E_{Fp}$):

$$n^0(\omega, \mu, T) = \begin{cases} \exp(\hbar\omega / (k_B T) - 1)^{-1}, & \hbar\omega < E_g \\ \exp((\hbar\omega - \mu) / (k_B T) - 1)^{-1}, & \hbar\omega \geq E_g \end{cases} \quad (2)$$

E_g is the gap energy, \hbar is the reduced Planck constant, ω the radiation angular frequency, k_B the Boltzmann constant and T the temperature.

In this work, we consider that the electrochemical potential μ is constant and equal to eU , a common approximation whose precision has been studied in [46]. By doing this approximation, we assume that the Bose-Einstein distribution is similar in all points of the LED (resp. PV cell), therefore that the net photon flux density between two points of the same device is null.

The other factor, $\mathcal{T}_{sl}(z_l)$, corresponds to an equivalent transmission coefficient between the layer s and any point of the layer l , and can be obtained from the transmission coefficient $\mathcal{T}_{sl}(z_s, z_l)$ between two points positioned respectively in layers s and l

$$\mathcal{T}_{sl}(z_l) = \int_{z_s} z'_s \mathcal{T}_{sl}(z'_s, z_l) dz'_s \quad (3a)$$

$$\mathcal{T}_{sl}(z_s, z_l) = \frac{k_v}{\pi^2} \Re \left(i \epsilon''_{r1} \int_0^{+\infty} F_{\omega,sl}(k_\rho) k_\rho dk_\rho \right) \quad (3b)$$

$$F_{\omega,sl}(k_\rho) = \begin{bmatrix} g_{sl\rho\rho}^E(\omega, k_\rho, z_s, z_l) g_{sl\theta\rho}^{H*}(\omega, k_\rho, z_s, z_l) \\ + g_{sl\rho z}^E(\omega, k_\rho, z_s, z_l) g_{sl\theta z}^{H*}(\omega, k_\rho, z_s, z_l) \\ - g_{sl\theta\theta}^E(\omega, k_\rho, z_s, z_l) g_{sl\rho\theta}^{H*}(\omega, k_\rho, z_s, z_l) \end{bmatrix}. \quad (3c)$$

The terms g correspond to the different Weyl components of the Green tensors, k_ρ is the parallel component of the wavevector \mathbf{k} , k_v is the vacuum wavenumber corresponding to the given frequency ω and ϵ'' is the imaginary part of the dielectric function ϵ .

In this work, we assume that the LED and PV cell temperatures are kept constant; thus, below-bandgap photons do not have any impact on the electrical performance, only on the device efficiency. In the following, the photon flux density γ_{sl} used in the electrical models is therefore defined as the integral of its spectral quantity over above-bandgap photons:

$$\gamma_{sl} = \gamma_{\hbar\omega \geq E_g, sl} = \int_{E_g/\hbar}^{+\infty} \gamma_{\omega,sl} d\omega.$$

2.2. Charge carrier behaviour

Once the spectral photon flux density γ_ω is obtained, the charge carrier behaviour can be modeled. In order to do so, we use two different methods:

- The detailed balance (DB) method (see Section 2.2.1) allows to easily obtain the current thanks to a balance between photons and charge carriers. This method has been used in the literature for the computation of the currents in a TPX device [18, 20, 30].
- The simplified drift-diffusion (SDD) method, in which the drift-diffusion equations are solved using standard approximations, is routinely used in photovoltaics [33, 34] but has not been used for TPX devices until now.

The use of these two methods allows for a complete description of the device performance. By using the DB method, we can estimate the ideal capabilities of such a system; then, thanks to the SDD method, the power output of a specific device can be obtained and its efficiency estimated in comparison to the ideal case.

2.2.1. Detailed balance (0D)

The photon flux density is known at any point of the system. In order to obtain a direct relation with the current densities, several assumptions have to be made [18]:

- absorption** - each above-bandgap photon absorbed generates a unique electron-hole (e-h) pair: $\tilde{G}_{rad} = \gamma_{abs} = \gamma_{sl}^{in}(z_l^-) - \gamma_{sl}^{in}(z_l^+)$ (defining $\tilde{x} = \int x dz$ and z_l^\pm as the limits of the layer considered).
- radiative recombination** - photon recycling is neglected, thus the local radiative recombination corresponds to the photon flux density emitted towards the other device: $\tilde{R}_{rad} = \gamma_{em} = \gamma_{sl}^{out}(z_l^-) - \gamma_{sl}^{out}(z_l^+)$.
- non-radiative recombination** - the level of non-radiative recombinations and of thermal generation of e-h pairs is set by the Internal Quantum Efficiency (IQE): $\tilde{R}_{nonrad} = (1/\text{IQE} - 1)\gamma_{em}$ and $\tilde{G}_{nonrad} = (1/\text{IQE} - 1)\gamma_{em}(U_l = 0)$.

Since $J = e(\tilde{G} - \tilde{R})$, we obtain

$$J_l = e \left[\gamma_{abs} - \gamma_{em} - \left(\frac{1}{IQE} - 1 \right) (\gamma_{em} - \gamma_{em}(U = 0)) \right] \\ = e \left[(\gamma_{sl}(z_l^-) - \gamma_{sl}(z_l^+)) - \left(\frac{1}{IQE} - 1 \right) \right. \\ \left. (n_l^0 - n_l^0(U_l = 0)) (\mathcal{T}_{sl}(z_l^-) - \mathcal{T}_{sl}(z_l^+)) \right]. \quad (4)$$

This expression can be simplified if $IQE = 1$:

$$J_l = e (\gamma_{sl}(z_l^-) - \gamma_{sl}(z_l^+)). \quad (5)$$

These two equations are developed in [18, 30]. In [20], a more thorough model has been developed. However, in the case of this work, we aim to obtain a simple and ideal (or quasi-ideal if $IQE < 1$) model, therefore refining the DB model is not of interest for us.

Note that when using the DB method, we consider that both devices (labeled respectively s and l) are homogeneous semi-infinite media for the radiative computation, i.e. that $\mathcal{T}_{sl}(z_l^+) \approx 0$ (thus $\gamma_{sl}(z_l^+) \approx 0$). This allows to obtain ideal or quasi-ideal performances which are independent of the LED and PV cell geometries considered. In addition, when considering quasi-ideal cases, the IQE chosen is identical for the LED and the PV cell.

2.2.2. Drift-Diffusion (1D)

For a thorough modelling of a TPX system, Poisson, continuity and drift-diffusion equations should be solved simultaneously in order to obtain the local charge carriers distribution n and p , electric field inside the junction E and electron and hole currents J_n and J_p . In 1D, these equations are expressed as

$$\frac{dE}{dz}(z) = -\frac{e}{\epsilon_s} (n(z) - p(z) + N_a(z) - N_d(z)) \quad (6)$$

$$\frac{dJ_n}{dz}(z) = e(R(z) - G(z)) \quad (7a)$$

$$\frac{dJ_p}{dz}(z) = -e(R(z) - G(z)) \quad (7b)$$

$$J_n(z) = e \cdot n(z)\mu_n E(z) + eD_n \frac{dn}{dz}(z) \quad (8a)$$

$$J_p(z) = e \cdot p(z)\mu_p E(z) - eD_p \frac{dp}{dz}(z). \quad (8b)$$

These equations being coupled, solving the complete problem would need to implement an iterative process [43, 47]. However, standard approximations are regularly used to simplify the problem [33, 34]:

- the depletion approximation, in which the electric field is analytically defined and becomes independent of the illumination.
- the low-injection approximation, in which we assume that the illumination is low enough to have constant majority carrier densities (equal to the doping level).

By using these approximations, the problem can be decoupled, obtaining one differential equation for the minority carrier density to be solved in the quasi-neutral regions on the p-side and on the n-side. This differential equation is expressed for electrons in the p-region as

$$D_n \frac{d^2 \Delta n_p}{dz^2}(z_p) - \frac{\Delta n_p(z_p)}{\tau_{non-rad,n}} + G(z_p) - R_{rad}(z_p) = 0. \quad (9)$$

In this equation, Δn_p represents the variation of the electron density in the p-region compared to the equilibrium value n_{p0} . z_p corresponds to the position in the p-region, and the differential equation should be solved between the limit of the depletion region in the p-region $z_{p,dp}$ and the boundary of the region t_p . The boundary conditions are

$$\Delta n_p(z_{p,dp}) = n_{p0} \left(\exp\left(\frac{eU}{k_B T}\right) - 1 \right) \quad (10a)$$

$$D_n \frac{d\Delta n_p}{dz}(t_p) = -S_n \Delta n_p(t_p). \quad (10b)$$

Note that the differential equation and the boundary conditions are identical for holes in the n-region. S_n corresponds to the surface recombination coefficient for electrons at the front interface (see Table 2). We consider equivalent surface recombinations at the front and back interfaces of the junctions: $S_p = S_n = 5 \times 10^2 \text{ m.s}^{-1}$. $D_{n,p}$ is the diffusion coefficient, obtained from the mobility $\mu_{n,p}$ through Einstein's equation:

$$D_{n,p} = \mu_{n,p} \cdot k_B T / e. \quad (11)$$

For the SDD method, as for the DB method, the generation of e-h pairs is computed from the results of the near-field radiative heat transfer model. Here, the two layers (p- and n-regions) of each device are considered for the radiative and charge transport computations, as shown in Figure 1. In order to have the localized photon flux density, it is therefore necessary to sum γ_{sl} over the two emission layers s , which can be those of the LED or of the PV cell depending on the device considered. In addition, the volumetric generation rate is needed instead of the global one, and can be written as

$$G_l = -\frac{d\gamma^{in}}{dz}(z_l). \quad (12)$$

Similarly, we write the radiative recombination rate as

$$R_{rad} = -\frac{d\gamma^{out}}{dz}(z_l). \quad (13)$$

Note that in the existing literature for TPV (including in the near-field), radiative recombinations are modeled either by using a radiative recombination coefficient B [17, 43] or by using an iterative process that allows for a precise modelling of photon recycling and transfer between the two bodies [46]. Of course, our modelling should tend towards precision (thus the second solution). However, in this work, we use an intermediary between these two models as shown in Eq. 13, which has several advantages:

1. compared to the use of a coefficient B , using the local emission rate for computing the radiative recombinations allows to account for the influence of the geometry and of near-field effects.
2. compared to the precise modelling, this method does not need any iteration, simplifying the calculations.
3. the expressions of the radiative generation and recombination rates are similarly expressed for the DB and the SDD methods, allowing for an easier comparison.

The carrier lifetime related to non-radiative recombinations $\tau_{non-rad}$ is computed using classic A and C coefficients (see Table 2), taking into account Shockley-Read-Hall (SRH) recombinations and Auger recombinations:

$$\tau_{non-rad} = (A + C \cdot N^2)^{-1} \quad (14)$$

Once the charge carrier densities are known, the current density can then be computed as:

$$J = J_n + J_p + J_{dp} \quad (15)$$

where J_n and J_p are the minority carrier current densities at the depletion region boundary (whose expression can be obtained from Eq. 8 by setting $E = 0$) and J_{dp} is the current related to the depletion region, given by (neglecting non-radiative recombinations due to the depletion approximation):

$$J_{dp} = e \int_{dp} (G(z) - R_{rad}(z)) dz \quad (16)$$

The doping levels selected in Table 1 have been chosen so that these approximations are valid: by taking as a reference the work from Blandre *et al.* [43], a doping level of 10^{17} cm^{-3} for both the p- and n-regions would be enough to consider that the system is in the low-injection regime. In order to ensure that the approximation is correct, we use larger doping levels: a donor doping level N_d of 10^{18} cm^{-3} and an acceptor doping level N_a of 10^{20} cm^{-3} . Since non-radiative recombinations are neglected in the depletion region (see Eq. 16), J_{dp} is only approached: therefore, if it becomes a predominant part of the current, this could increase the error made by using the SDD model and require the use of a more precise model. For the geometries considered in this paper (see Table 1), J_{dp} only accounts for 1 to 10% of the total current density, because the doping levels are high enough to keep the depletion region thin (of the order of tens of nanometers). We thus expect the SDD model to be precise enough for these different cases.

3. Analysis of the reference case

3.1. Absorption and Emission

Before looking at the performance of a NF-TPX device, it is interesting to study the net absorption and emission profiles at a 10 nm gap distance, respectively for the LED and the PV cell. The profiles obtained with the reference case (see Table 1) are shown in Figure 2.

Looking first at above-bandgap quantities, which are the most important for power generation, we observe as expected an extremely large increase in the absorption and emission rates, with the mean increase factor from the far-field (FF) case to the near-field (NF) case with electroluminescent enhancement (for LED and PV cell voltages of 1 V) reaching 10^9 . Most of this increase is due to electroluminescence: going to the near-field only accounts for a mean increase rate of the order of 10. The dramatic effect of electroluminescence on the radiative heat transfer however comes with an increased electrical power consumption, and does not necessarily cause an increase in the net power density produced. This will be discussed in Section 3.3.

In the insets of Figures 2a and 2b are shown the total emission and absorption rates. Their variations are quite different compared to their above-bandgap equivalent. First, the rates abruptly change at the p-n boundary: because the doping levels and the majority carriers are different, the dielectric functions obtained with the Drude model (see Table 2) are different for the p and n layers, causing the photons to be reflected back and causing the emission (or absorption) discontinuity.

The rates of increase between the three cases studied are also quite different. Near-field effects allow for a much larger increase, up to 10^4 at the front surface. Meanwhile, the impact of electroluminescence is nearly negligible, since the orange and yellow curves are almost superimposed. This can be better seen using Figures 2c and 2d, where the spectral emission and absorption rates are shown. Two regions can be distinguished:

- a) a first one in the infrared (below 0.3 eV, hence above 4 μm), corresponding to the usual photon energy range of radiation for bodies close to room temperature
- b) a second one in the visible (between 1.42 and 2 eV, hence between 600 and 900 nm), corresponding to the electrically-induced emission/absorption (i.e., electroluminescence).

As the electroluminescent peak is low compared to the thermal peak (see Figure 2e), we cannot see the influence of the voltage on the total rates. One can notice the similarity between the LED emission and the PV cell absorption profiles. These two profiles are indeed symmetrical, because of the device symmetry (in terms of geometry, of optical properties and of doping levels).

3.2. Parametric Study

We now investigate the global influence of two key parameters, the LED temperature and the gap distance, on the ideal performance achievable by a GaAs NF-TPX device. In order to do so, we perform a parametric study using the DB method around the reference case (see Table 1). Results are reported in Figure 3. The LED temperature impact on the device is computed for two different IQEs of 1 and 0.9 (frequency and temperature independent). In the ideal scenario (IQE = 1), it is shown to have only limited effect on the power output, with an increase rate of a factor 2 between 550 K and 650 K. However, this increase is much

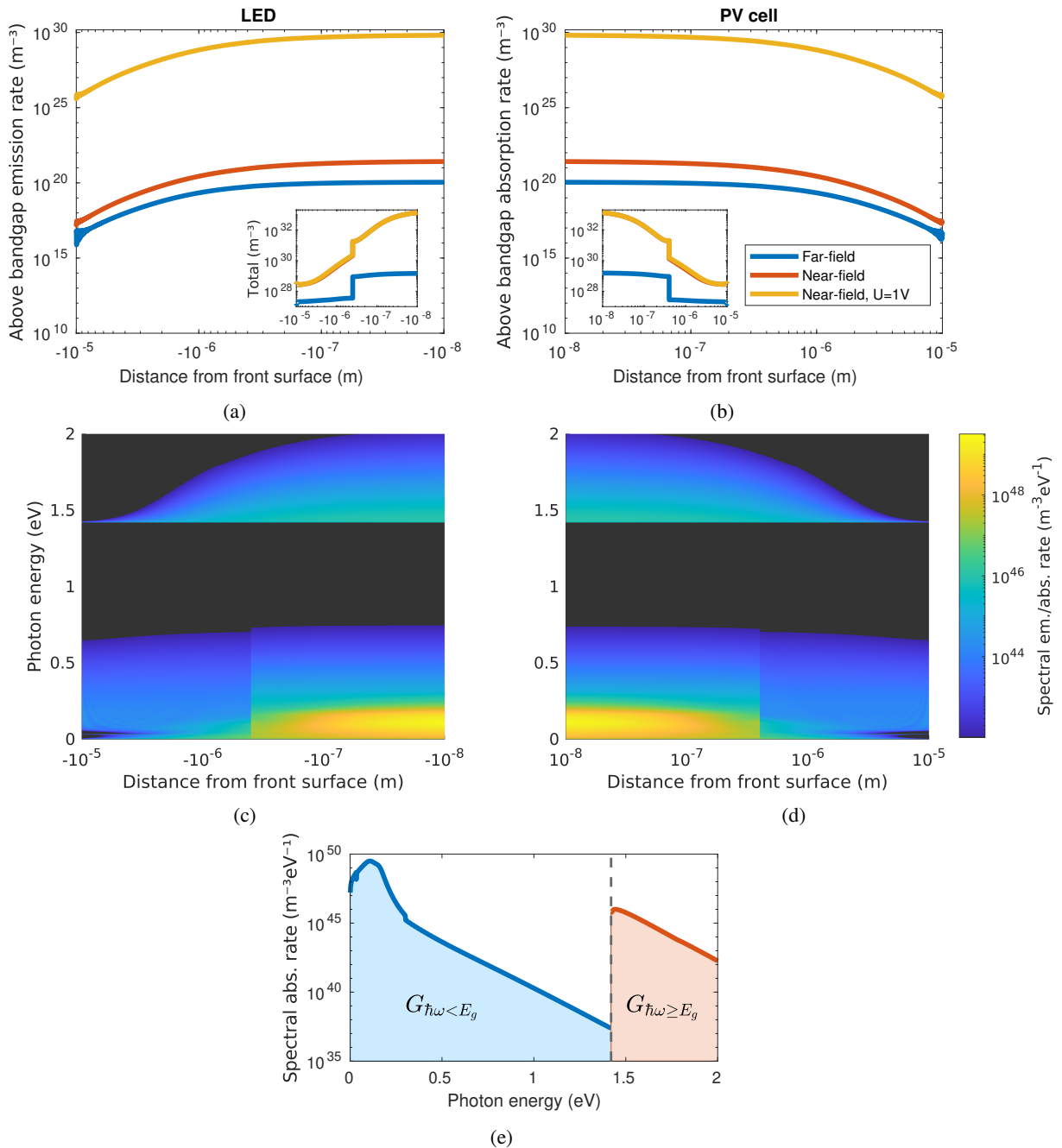


Figure 2: (a) LED emission profile and (b) PV cell absorption profile of above-bandgap photons in the far-field (blue), in the near-field (orange) and in the near-field with electroluminescence, for LED and PV voltages of 1 V (yellow). Profiles obtained with all photons (below and above bandgap) are shown in insets. The spectral profiles obtained in the near field with electroluminescence are shown for the LED and the PV cell respectively in (c) and (d), for different depths. The corresponding profile at the front surface of the PV cell is shown in (e).

larger for lower IQE, reaching a factor 16 in the same range of temperature for $\text{IQE} = 0.9$. This shows the importance of using devices with nearly ideal IQE for low temperature application, as stated in the introduction.

In Figure 3b is shown the influence of the gap distance on the above-bandgap radiative heat flux and on the different electrical powers involved, for an IQE of 0.9. As shown in [48], it is interesting to study the variation of amplitude of

the different modes composing the heat flux, i.e. propagative modes, frustrated modes (which propagate in GaAs but are evanescent in vacuum) and surface modes (which are evanescent on each side of the interface). Three different regions can be observed:

- above a few microns: it is the FF regime, with constant values for the different powers.

- b) between hundreds of nanometers and a few microns: propagative modes are still dominant in the radiative heat flux, but cavity effects cause oscillations of the powers around the far-field value.
- c) below hundreds of nanometers: frustrated evanescent modes become dominant, causing a large increase of the powers at first, before a slower increase below tens of nanometers. At 1 nm, surface modes are still in minority, but have exceeded propagative modes.

Looking more closely at the power levels consumed by the LED and produced by the PV cell, we can note their proximity, caused by an IQE already far from the ideal case and causing the net power output to be quite small compared to them.

By computing the ratio between the radiative heat flux exchanged and the electrical power produced or consumed, we can obtain an estimation of the conversion efficiencies at maximum power. We first focus on above-bandgap photons. Above-bandgap efficiencies are nearly independent of the gap distance, reached at the same voltages for any of the gap

distance considered ($U_{LED} = 1.00\text{V}$ and $U_{PV} = 1.16\text{V}$), and equal to

$$\eta_{PV,light-el} = \frac{P_{PV}}{q_{\hbar\omega \geq E_g}} = 78\%, \quad (17a)$$

$$\eta_{LED,el-light} = \frac{q_{\hbar\omega \geq E_g}}{P_{LED}} = 132\%, \quad (17b)$$

showing thus the quality of the conversions of each device. Note that the efficiency is greater than 1 for the LED because it is heated: it will still have a positive net emission even with no electrical power consumed. Since most of the power produced by the PV cell is sent back to the LED, the net conversion efficiency is much lower:

$$\eta_c = \frac{P_{net}}{q_{\hbar\omega \geq E_g}} = 2\%. \quad (18)$$

This net conversion efficiency should not be confused with the efficiency of the device, which would be expressed as the ratio between the device power output and the heat supplied to the LED in order to keep its temperature constant. We obtain

$$\eta_\Sigma = \frac{P_{net}}{q_{\hbar\omega \geq E_g} - P_{LED}} = 9\%. \quad (19)$$

equivalent to a scaled efficiency (i.e. the efficiency divided by the related Carnot efficiency) of 18%, close to what is found for NF-TPV (e.g., 23% in [17]). These results are obtained for above-bandgap photons, providing an upper bound for the overall efficiency.

A complete evaluation of the efficiency is performed at $d = 10\text{ nm}$. We model GaAs dielectric function below the bandgap with a decoupled Drude-Lorentz model. Most of the values needed in this model are given or can be computed thanks to [39]; for the variation of the Drude damping coefficient, we use the expression given in [40]. However, since the Drude model depends on the doping levels, we have to consider a specific geometry. By taking the reference case, the junctions are thick enough so that the hypothesis of semi-infinite junctions remains true. The power densities are thus similar to those computed above.

The results obtained are provided in Table 3: as shown in the previous section, below-bandgap photons still dominate the photon flux for an IQE of 0.9, worsening therefore the different efficiencies and increasing the heating (resp. cooling) power required to keep the LED (resp. the PV cell) at constant temperature. While only 10^4 W.m^{-2} are needed when considering above-bandgap photons, this rises up to 10^6 W.m^{-2} by considering all photons. This underlines the thermal management issue of such devices.

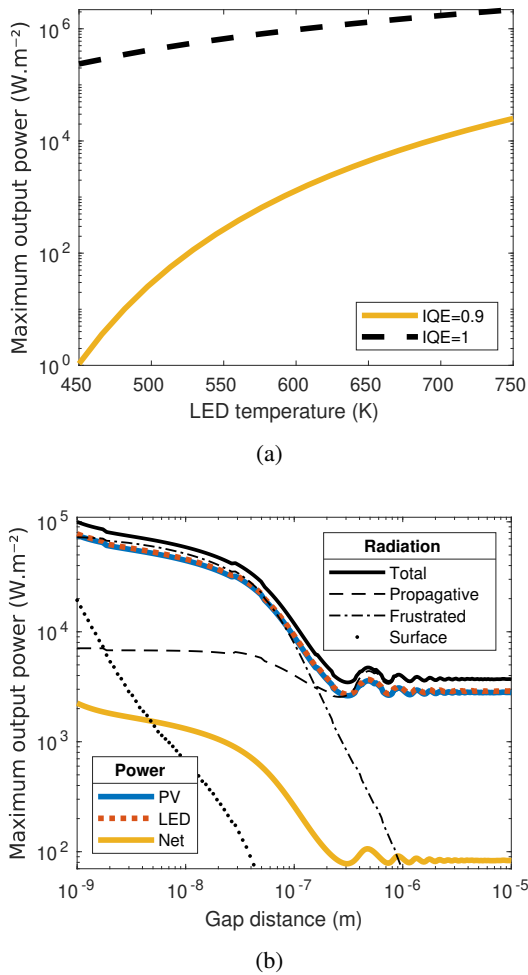


Figure 3: Influence of (a) the LED temperature and (b) the gap distance on the power produced by the device. For both cases, the parametric analysis is performed around the reference case. In (b), an IQE of 0.9 is considered.

Table 3

Device efficiency for a 10 nm gap distance.

	q ($\text{W}\cdot\text{m}^{-2}$)	η_{PV} (%)	η_{LED} (%)	η_c (%)	η_Σ (%)
Above E_g	5.9×10^4	78	1.3×10^2	2.2	9.1
All photons	1.3×10^6	3.5	2.9×10^3	9.9×10^{-2}	1.0

3.3. I-V and P-V characteristics

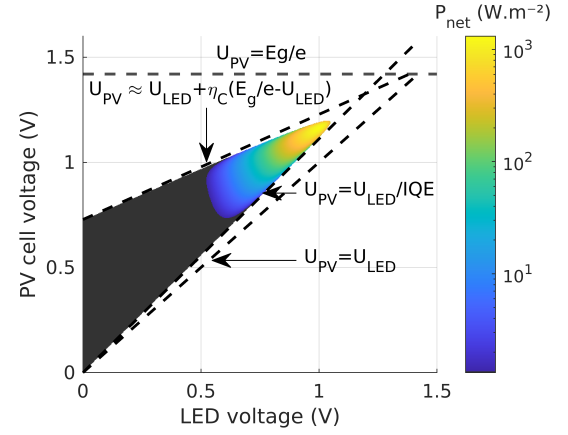
We now look at the characteristics obtained for a NF-TPX device, starting with the results obtained with the DB method for an IQE of 0.9 (Figure 4a). Since both the LED and the PV cell voltages vary, the characteristic of a NF-TPX device is a 3D plot. The region in which the net electrical power output is positive is strictly limited by two inequalities:

- $U_{LED} \leq U_{PV}$: with the hypothesis considered, we always have $|J_{LED}| \geq |J_{PV}|$ (they are equal if IQE = 1), having as a consequence that U_{PV} must be greater than U_{LED} in order to produce electrical power.
- $U_{PV} < E_g/e$: if the voltage reaches this value, the modified Bose-Einstein distribution diverges.

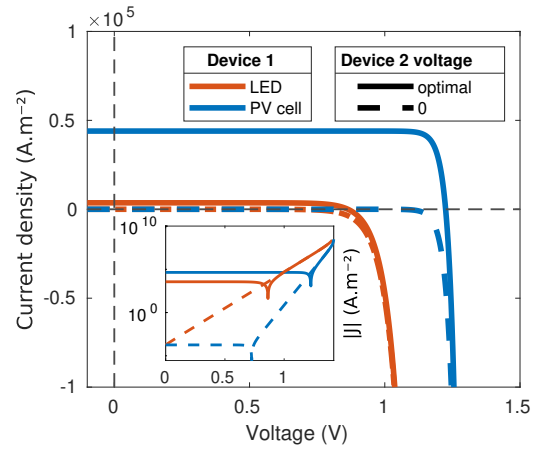
Even if the characteristic is limited by these two inequalities, other phenomena determine where power can be extracted from the device. For a given LED voltage, if the PV cell voltage is too large, electroluminescence from the PV cell is important enough to counterbalance the difference of temperature with the LED and change the direction of the net radiative heat flux. In addition, when decreasing the IQE, the range of acceptable PV cell voltage for a given LED voltage becomes narrower, resulting in the decrease of the power output. If the maximum power point (MPP) of an ideal device is close to the point $(E_g/e, E_g/e)$, the real MPP is located at lower voltages. A quick estimation of its location can be found at the intersection of two straight lines that qualitatively envelop the characteristic of the device with a good precision and correspond to the two limiting factors stated above:

- $U_{PV} = U_{LED} + \eta_c (E_g/e - U_{LED}) + k_B T_{PV}/e \cdot \ln(T_{LED}/T_{PV})$: balance between thermally- and electrically-induced emission for the LED and the PV cell (η_c corresponds to the Carnot efficiency). This expression is derived from $\gamma = 0$, which can be reduced to $\Delta n^0 = 0$ by assuming a constant transmission coefficient. As a first approximation, the last term of the equation can be neglected.
- $U_{PV} = U_{LED}/\text{IQE}$: reduction of the PV cell voltage range available with the IQE.

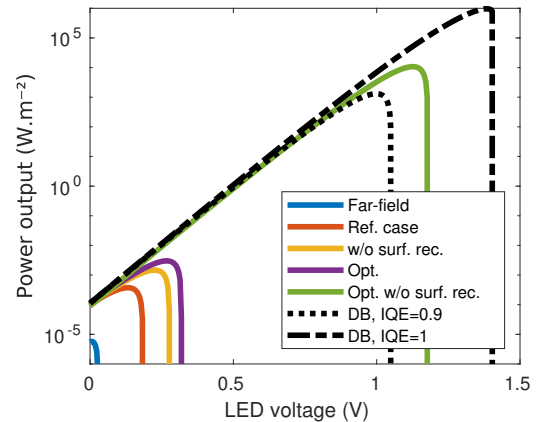
In Figure 4b, we show the I-V curve of the LED and the PV cell. The voltage given on the horizontal axis is, respectively, the LED voltage and the PV cell voltage. For the LED (resp. the PV cell) characteristic, the PV cell (resp. the LED) voltage is kept either at its optimum value (i.e. $U_{PV} = 1.16$ V and $U_{LED} = 1$ V) or at 0. For the PV cell, increasing the LED voltage (from the dashed blue line



(a)



(b)



(c)

Figure 4: (a) Full V-V characteristic of the device, obtained with the 0D model and for an IQE of 0.9. Precise expression of the upper limit is given in the text. (b) I-V characteristics of the LED and the PV cell around the maximum power point from (a). (c) Simplified P-V characteristics of the device, where the power is computed from the full characteristics as $P(U_{LED}) = \max P(U_{LED}, U_{PV}), 0 \leq U_{PV} < E_g/e$. See Section 4 for an explanation on the optimization.

to the full blue line) raises significantly the short-circuit current by means of electroluminescence. For the LED, we can notice that the variation of the characteristic with the PV cell voltage (from the dashed orange line to the full orange line) is slower; however, for low LED voltage, electroluminescence from the PV cell is large enough to reverse the direction of the net heat flux, thus changing the sign of the short-circuit current and allowing for a power production from the LED. In this case (low LED voltage, high PV cell voltage), the LED works as a PV cell while the PV cell works as a LED. In fact, this regime where the high-temperature device is also the high-voltage device corresponds to the heat-pump/refrigerator configuration of the NF-TPX device.

In order to ease the understanding, we use simplified characteristics in the following, as shown in Figure 4c. In this case, we plot the variation of the power output only with respect to the LED voltage. For each LED voltage, we take the maximum power output reached for the PV cell voltages considered: $P(U_{LED}) = \max P(U_{LED}, U_{PV}), 0 \leq U_{PV} < E_g/e$. This way of presenting the performance has several advantages:

- the comparison of the characteristic of different devices is made easier,
- the maximum power produced by the TPX device, along with the power produced by the related TPV device (at $U_{LED} = 0$), is made more readable.

In black is traced the characteristic obtained with the DB method, for an IQE of 0.9 and 1, with respective maximum output powers of $P_{IQE=0.9} = 1.3 \times 10^3 \text{ W.m}^{-2}$ and $P_{IQE=1} = 9.7 \times 10^5 \text{ W.m}^{-2}$. Two main domains can be observed, with a fairly linear evolution first, and a sudden decrease in the electrical power output due to the exponential variations caused by the Bose-Einstein distributions. It is also interesting to note that for an IQE of 0.9, the characteristic is nearly identical to the one obtained for IQE = 1 up to a LED voltage of 0.9 V, meaning that the reduction of the power output seems to be mainly affected by the reduction of the achievable voltage range.

In color are then plotted the results obtained with the SDD method, in the FF (blue) and in the NF (orange). The maximum performance of the device is given respectively as $P_{FF} = 5.8 \times 10^{-6} \text{ W.m}^{-2}$ and $P_{NF} = 3.7 \times 10^{-4} \text{ W.m}^{-2}$. Even in the NF, the performance of the device considered is mediocre. Still, using TPX instead of TPV (i.e., with $U_{LED} = 0 \text{ V}$) shows a quite noteworthy improvement ($P_{NF-TPX}/P_{NF-TPV} \simeq 4$). The different maximum power outputs and their respective LED and PV cell voltages are summarized in Table 4.

In the next section, we will thus focus on the understanding of the difference in the results obtained between the DB and the SDD methods, before trying to improve the device considered.

4. Towards improved devices

Table 4

Maximum power point reached for the different cases studied in Figure 4c.

Method	Case	P (W.m ⁻²)	U _{LED} (V)	U _{PV} (V)
SDD	Far-field	5.8×10 ⁻⁶	0.00	0.58
	Ref. case	3.7×10 ⁻⁴	0.13	0.69
	W/o surf. rec.	1.5×10 ⁻³	0.22	0.75
	Optimized	3.0×10 ⁻³	0.27	0.77
DB	Opt. w/o surf. rec.	1.1×10 ⁴	1.13	1.25
	IQE = 0.9	1.3×10 ³	1.00	1.16
	IQE = 1	9.7×10 ⁵	1.38	1.4

4.1. Surface recombinations

A first means to increase the performance of the device is to decrease surface recombinations. By nature, these are non-idealities caused by the device (i.e., not necessarily directly related to a given material) that limit the collection of charges. In Figure 4c, we show the P-V characteristic obtained when surface recombinations are removed (in yellow). If this allows for moderate improvement, with the maximum power output increased by a factor 4 compared to the reference case and reaching $P_{S=0} = 1.5 \times 10^{-3} \text{ W.m}^{-2}$, reducing the surface recombinations is still important to approach quasi-ideal and ideal cases as will be discussed in Section 4.3.

4.2. Carrier diffusion length

Two other parameters of interest could be studied in order to search for improved performance: the carriers diffusion coefficient D (Eq. 11) and the non-radiative lifetime τ (Eq. 14). Unlike surface recombinations coefficients, these two parameters are physically only related to the material and thus cannot be changed easily. However, they provide good information about the charge carrier movement capabilities inside the device, through the diffusion length $L_{diff} = \sqrt{D\tau}$. By varying L_{diff} , we modify the distance carriers will be able to travel, a process which is thus equivalent to changing the geometry for electrons and holes, but not for photons. By doing this theoretical analysis, we can easily observe how close we could approach the ideal case; this provides information about what could be obtained when optimizing the geometry. For the sake of simplicity, this study is performed separately for the LED and the PV cell, with the other device kept as a passive emitter or receiver. We choose to change the diffusion length around the value $L_{diff,0}$ obtained using the physical parameters from Table 2. Since both D and τ change when the diffusion length varies, we force them to vary at the same rate: $L_{diff} = \sqrt{(F_L \cdot D_0)(F_L \cdot \tau_0)} = F_L L_{diff,0}$. The results, shown in Figure 5, reveal that the I-V characteristic of the two devices tends towards the ideal case when the diffusion lengths considered reach a hundred times the physical value. By a really rough approximation, we could state that increasing the diffusion length by a factor F_L is similar to decreasing the geometry by the same factor. While it is probably not possible to decrease all the dimensions by a factor 100, we

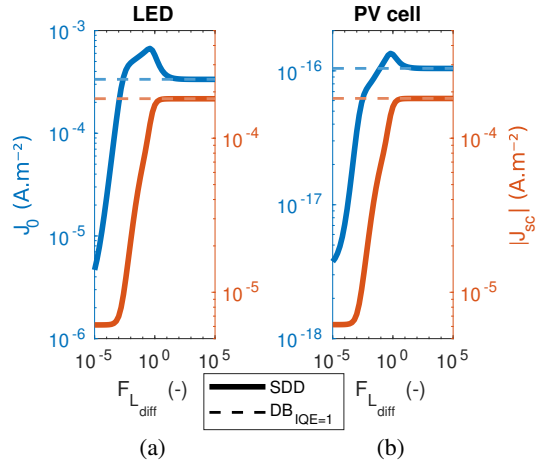


Figure 5: Impact of the diffusion length L_{diff} on the dark current and the short-circuit current of (a) an LED at 600 K, facing a GaAs absorber at 300 K and (b) a PV cell at 300 K facing a GaAs emitter at 600 K. Since the value of the diffusion length changes in the p-region and in the n-region, the variation of the dark current is shown as a function of the factor F_L defined as $L_{diff} = F_L L_{diff,0}$. Similar tendencies are found for the short-circuit current.

can however note that the dark current is already quite close to the ideal value for $F_L = 10$.

4.3. Improving the geometry

We now try to optimize the geometry in order to see if we could approach the ideal case. This optimization is performed using the *fmincon* solver of MATLAB, an algorithm searching for local minima; if this solution would not be relevant for finding the optimal geometry, since the result of the process can vary with the starting point, it however returns geometries that are improved in comparison to the reference case.

We set the thickness for each region in the range [10 nm; 10 μ m], while eliminating surface recombinations. The result of this early optimization process is given in Figure 4c (green), while the improved geometry parameters are given in Table 1. The maximum power output is much larger than those obtained for all the other cases, reaching a value of $P_{opt,S=0} = 1.1 \times 10^4$ W.m⁻². It even exceeds what was obtained with the DB method for a quasi-ideal NF-TPX device with an IQE of 0.9, and the performance reached by a FF-TPV device with an emitter at more than 1400 K [11]. It is also close to what is found for NF-TPV for 700 K temperature difference [49], and for thermoelectric devices for 300 K temperature difference [50]. This result is invigorating for the development of NF-TPX device: it shows that even when getting rid of idealizing approximations, we can reach really high electrical power densities by improving both the contacts at the boundaries of the LED and the PV cell and their geometries for efficient charge carrier management. The device performance could be even further improved by optimizing the doping level of the different layers; however, the use of the SDD method limits the range

of doping levels for which the result obtained is accurate. Solving instead the full set of equations (see Eq. 6,7 and 8) would permit a correct optimization of the doping levels.

It is important to notice that the improvement of the geometry alone would not allow for such a large increase of the power output: when optimizing the geometry while keeping surface recombinations on the front surface (in purple in Figure 4c, see Table 1 for the geometry obtained), we reach $P_{opt} = 3.0 \times 10^{-3}$ W.m⁻², in the same order of magnitude as what was found using the reference case without surface recombinations.

The optimized geometry exhibits p-regions that are only 10 nm thin (i.e., the lower bound of the thickness range tested); if reaching such thickness seems difficult to achieve, it highlights nonetheless the necessity to reduce the thickness of the front layer in order to achieve high performance.

In Figure 6, we show the variation of electric field, electrostatic potential and quasi Fermi levels inside the LED and the PV cell, at the MPP. We notice that the quasi-Fermi levels (in color in Figures 6e and 6f) are nearly constant: the assumption that the electrochemical potential is nearly constant and equal to eU seems therefore valid for this specific case.

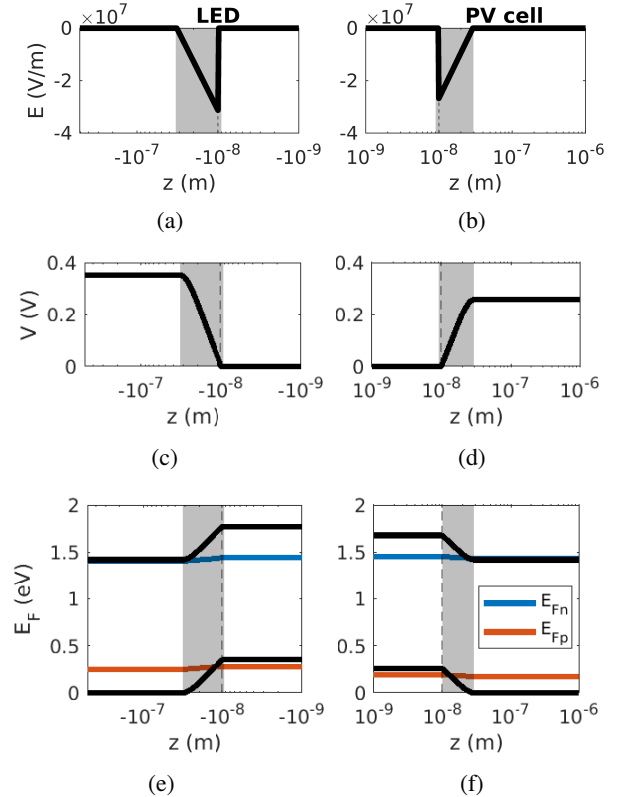


Figure 6: (a,b) Electric field, (c,d) Electrostatic potential and (e,f) Quasi-Fermi levels of the LED and the PV cell composing the device at the maximum power point reached without surface recombinations, with the optimized geometry at 10 nm. The depletion region is represented in grey.

5. Conclusion and Outlooks

We have developed a model coupling near-field radiative heat transfer and charge carrier transport using the simplified drift-diffusion method, allowing for an accurate representation of the phenomena occurring in a near-field thermophotonic device. The difference between the results obtained with the Detailed Balance (in 0D) and the simplified drift-diffusion (in 1D) methods underlines the necessity to use the latter for a precise estimation of a device performance. By carrying an extensive analysis of a GaAs-based near-field thermophotonic device, we have also identified that the diffusion length and the surface recombinations have strong impacts on the performance. Through the improvement of the contacts and of the geometry, we are capable of reaching power densities as high as $P = 1.1 \times 10^4 \text{ W.m}^{-2}$, i.e. close to $35 \text{ W.m}^{-2}.\text{K}^{-1}$. This is a promising result for near-field thermophotonic devices, especially since such performance was obtained in spite of the high GaAs bandgap energy compared to thermal energy at 600 K. In addition, the doping concentrations are fixed in this study, thus not optimized. Of course, the numerical study developed above has still room for improvement. In future work, the model itself should be improved, by getting rid of the approximation $\mu = eU$ in the modified Bose-Einstein distribution (see Eq. 2) and by solving fully the Poisson, drift-diffusion and continuity equations (see Eq. 6,7,8) instead of using the simplified drift-diffusion method. These developments have already been addressed for near-field thermophotovoltaic applications respectively in [46] and [43], and could be applied to near-field thermophotonics, allowing for an accurate description of the photon recycling and of the charge carrier behaviour in general. Apart from the algorithm itself, the device considered could also be modified to approach more realistic geometries, by considering the use of pin junctions [51] for instance.

Acknowledgements

We thank E. Blandre for the help given, P. Kivisaari, T. Sadi, J. Oksanen from Aalto University for constructive discussion, and E.J. Tervo for clarification.

The project TPX-Power has received funding from the European Union's Horizon 2020 research and innovation programme under grant agreement No. 951976.

References

- [1] Green, M.A., Bremner, S.P., 2016. Energy conversion approaches and materials for high-efficiency photovoltaics. *Nature Materials* 16, 23–34.
- [2] Melnick, C., Kaviani, M., 2019. From thermoelectricity to phonoelectricity. *Applied Physics Reviews* 6, 021305.
- [3] Chen, Z., Zhang, X., Pei, Y., 2018. Manipulation of Phonon Transport in Thermoelectrics. *Advanced Materials* 30, 1705617.
- [4] Mao, J., Liu, Z., Zhou, J., Zhu, H., Zhang, Q., Chen, G., Ren, Z., 2018. Advances in thermoelectrics. *Advances in Physics* 67, 69–147.
- [5] Daneshvar, H., Prinja, R., Kherani, N.P., 2015. Thermophotovoltaics: Fundamentals, challenges and prospects. *Applied Energy* 159, 560–575.
- [6] Schwede, J.W., Bargatin, I., Riley, D.C., Hardin, B.E., Rosenthal, S.J., Sun, Y., Schmitt, F., Pianetta, P., Howe, R.T., Shen, Z.X., Melosh, N.A., 2010. Photon-enhanced thermionic emission for solar concentrator systems. *Nature Materials* 9, 762–767.
- [7] Campbell, M.F., Celenza, T.J., Schmitt, F., Schwede, J.W., Bargatin, I., 2021. Progress Toward High Power Output in Thermionic Energy Converters. *Advanced Science* 8, 2003812.
- [8] König, D., Casalenuovo, K., Takeda, Y., Conibeer, G., Guillemoles, J.F., Patterson, R., Huang, L.M., Green, M.A., 2010. Hot carrier solar cells: Principles, materials and design. *Physica E: Low-Dimensional Systems and Nanostructures* 42, 2862–2866.
- [9] Li, M., Fu, J., Xu, Q., Sum, T.C., 2019. Slow Hot-Carrier Cooling in Halide Perovskites: Prospects for Hot-Carrier Solar Cells. *Advanced Materials* 31, 1802486.
- [10] Sakakibara, R., Stelmakh, V., Chan, W.R., Ghebrehan, M., Joannopoulos, J.D., Soljačić, M., Čelanović, I., 2019. Practical emitters for thermophotovoltaics: a review. *Journal of Photonics for Energy* 9, 032713.
- [11] Fan, D., Burger, T., McSherry, S., Lee, B., Lenert, A., Forrest, S.R., 2020. Near-perfect photon utilization in an air-bridge thermophotovoltaic cell. *Nature* 586, 237–241.
- [12] Tervo, E.J., Bagherisereshki, E., Zhang, Z.M., 2018. Near-field radiative thermoelectric energy converters: a review. *Frontiers in Energy* 12, 5–21.
- [13] Datas, A., 2016. Hybrid thermionic-photovoltaic converter. *Applied Physics Letters* 108, 143503.
- [14] Zeneli, M., Bellucci, A., Sabbatella, G., Trucchi, D.M., Nikolopoulos, A., Nikolopoulos, N., Karellas, S., Kakaras, E., 2020. Performance evaluation and optimization of the cooling system of a hybrid thermionic-photovoltaic converter. *Energy Conversion and Management* 210, 112717.
- [15] Whale, M.D., Cravalho, E.G., 2002. Modeling and performance of microscale thermophotovoltaic energy conversion devices. *IEEE Transactions on Energy Conversion* 17, 130–142.
- [16] Park, K., Basu, S., King, W.P., Zhang, Z.M., 2008. Performance analysis of near-field thermophotovoltaic devices considering absorption distribution. *Journal of Quantitative Spectroscopy and Radiative Transfer* 109, 305–316.
- [17] Francoeur, M., Vaillon, R., Meng, M.P., 2011. Thermal impacts on the performance of nanoscale-gap thermophotovoltaic power generators. *IEEE Transactions on Energy Conversion* 26, 686–698.
- [18] Harder, N.P., Green, M.A., 2003. Thermophotonics. *Semiconductor Science and Technology* 18, S270–S278.
- [19] Zhao, B., Buddhiraju, S., Santhanam, P., Chen, K., Fan, S., 2019. Self-sustaining thermophotonic circuits. *Proceedings of the National Academy of Sciences of the United States of America* 116, 11596–11601.
- [20] Zhao, B., Santhanam, P., Chen, K., Buddhiraju, S., Fan, S., 2018. Near-Field Thermophotonic Systems for Low-Grade Waste-Heat Recovery. *Nano Letters* 18, 5224–5230.
- [21] Zhang, Z.M., 2007. *Nano/Microscale heat transfer*. McGraw Hill.
- [22] Fiorino, A., Zhu, L., Thompson, D., Mittapally, R., Reddy, P., Meyhofer, E., 2018. Nanogap near-field thermophotovoltaics. *Nature Nanotechnology* 13, 806–811.
- [23] Inoue, T., Koyama, T., Kang, D.D., Ikeda, K., Asano, T., Noda, S., 2019. One-Chip Near-Field Thermophotovoltaic Device Integrating a Thin-Film Thermal Emitter and Photovoltaic Cell. *Nano Letters* 19, 3948–3952.
- [24] Bhatt, G.R., Zhao, B., Roberts, S., Datta, I., Mohanty, A., Lin, T., Hartmann, J.M., St-Gelais, R., Fan, S., Lipson, M., 2020. Integrated near-field thermo-photovoltaics for heat recycling. *Nature Communications* 11, 2545.
- [25] Lucchesi, C., Cakiroglu, D., Perez, J.P., Talierno, T., Tournié, E., Chapuis, P.O., Vaillon, R., 2021. Near-Field Thermophotovoltaic Conversion with High Electrical Power Density and Cell Efficiency

- above 14%. *Nano Letters* 11, 4524–4529.
- [26] Mittapally, R., Lee, B., Zhu, L., Reihani, A., Lim, J.W., Fan, D., Forrest, S.R., Reddy, P., Meyhofer, E., 2021. Near-field thermophotovoltaics for efficient heat to electricity conversion at high power density. *Nature Communications* 12, 4364.
- [27] Inoue, T., Ikeda, K., Song, B., Suzuki, T., Ishino, K., Asano, T., Noda, S., 2021. Integrated Near-Field Thermophotovoltaic Device Overcoming Blackbody Limit. *ACS Photonics* 8, 2466–2472.
- [28] Oksanen, J., Tulkki, J., 2010. Thermophotonic heat pump—a theoretical model and numerical simulations. *Journal of Applied Physics* 107, 093106.
- [29] Sadi, T., Radevici, I., Kivisaari, P., Oksanen, J., 2019. Electroluminescent Cooling in III-V Intracavity Diodes: Efficiency Bottlenecks. *IEEE Transactions on Electron Devices* 66, 2651–2656.
- [30] Sadi, T., Radevici, I., Oksanen, J., 2020. Thermophotonic cooling with light-emitting diodes. *Nature Photonics* 14, 205–214.
- [31] Bender, D.A., Cederberg, J.G., Wang, C., Sheik-Bahae, M., 2013. Development of high quantum efficiency GaAs/GaInP double heterostructures for laser cooling. *Applied Physics Letters* 102, 252102.
- [32] Vaillon, R., Parola, S., Lamnatou, C., Chemisana, D., 2020. Solar Cells Operating under Thermal Stress. *Cell Reports Physical Science* 1, 100267.
- [33] Nelson, J., 2003. *The Physics of Solar Cells*. Imperial College Press.
- [34] Kitai, A., 2011. *Principles of Solar Cells, LEDs and Diodes: The role of the PN junction*. Wiley.
- [35] Maros, A., Gangam, S., Fang, Y., Smith, J., Vasileska, D., Goodnick, S.M., Bertoni, M.I., Honsberg, C.B., 2015. High temperature characterization of GaAs single junction solar cells. 2015 IEEE 42nd Photovoltaic Specialist Conference, PVSC 2015 .
- [36] Sun, Y., Faucher, J., Jung, D., Vaisman, M., McPheeters, C., Sharps, P., Perl, E., Simon, J., Steiner, M., Friedman, D.J., Lee, M.L., 2017. Thermal stability of GaAs solar cells for high temperature applications. 2017 IEEE 44th Photovoltaic Specialist Conference (PVSC) , 2385–2388.
- [37] Gonzalez-Cuevas, J.A., Refaat, T.F., Abedin, M.N., Elsayed-Ali, H.E., 2007. Calculations of the temperature and alloy composition effects on the optical properties of $\text{Al}_x\text{Ga}_{1-x}\text{As}_y\text{Sb}_{1-y}$ and $\text{Ga}_x\text{In}_{1-x}\text{As}_y\text{Sb}_{1-y}$ in the spectral range 0.5–6 eV. *Journal of Applied Physics* 102, 014504.
- [38] Adachi, S., 1988. Optical properties of $\text{Al}_x\text{Ga}_{1-x}\text{As}$ alloys. *Physical Review B* 38, 12345–12352.
- [39] Adachi, S., 1994. *GaAs and Related Materials*. World Scientific.
- [40] Losego, M.D., Efremenko, A.Y., Rhodes, C.L., Cerruti, M.G., Franzen, S., Maria, J.P., 2009. Conductive oxide thin films: Model systems for understanding and controlling surface plasmon resonance. *Journal of Applied Physics* 106, 024903.
- [41] Ioffe Physico-Technical Institute, . Electronic archive on semiconductor materials.
- [42] Sotoodeh, M., Khalid, A.H., Rezazadeh, A.A., 2000. Empirical low-field mobility model for III-V compounds applicable in device simulation codes. *Journal of Applied Physics* 87, 2890–2900.
- [43] Blandre, E., Chapuis, P.O., Vaillon, R., 2017. High-injection effects in near-field thermophotovoltaic devices. *Scientific Reports* 7, 15860.
- [44] Rytov, S.M., Kravstov, Y.A., Tatarskii, Y.I., 1989. *Principles of Statistical Radiophysics*. Springer-Verlag.
- [45] Francoeur, M., Pinar Mengüç, M., Vaillon, R., 2009. Solution of near-field thermal radiation in one-dimensional layered media using dyadic Green's functions and the scattering matrix method. *Journal of Quantitative Spectroscopy and Radiative Transfer* 110, 2002–2018.
- [46] Callahan, W.A., Feng, D., Zhang, Z.M., Toberer, E.S., Ferguson, A.J., Tervo, E.J., 2021. Coupled Charge and Radiation Transport Processes in Thermophotovoltaic and Thermoradiative Cells. *Physical Review Applied* 15, 054035.
- [47] Gummel, H.K., 1964. A Self-Consistent Iterative Scheme for One-Dimensional Steady State Transistor Calculations. *IEEE Transactions on Electron Devices* 11, 455–465.
- [48] Bernardi, M.P., Dupré, O., Blandre, E., Chapuis, P.O., Vaillon, R., Francoeur, M., 2015. Impacts of propagating, frustrated and surface modes on radiative, electrical and thermal losses in nanoscale-gap thermophotovoltaic power generators. *Scientific Reports* 5, 11626.
- [49] Vaillon, R., Perez, J.P., Lucchesi, C., Cakiroglu, D., Chapuis, P.O., Taliercio, T., Tournié, E., 2019. Micron-sized liquid nitrogen-cooled indium antimonide photovoltaic cell for near-field thermophotovoltaics. *Optics Express* 27, A11–A24.
- [50] El Oualid, S., Kogut, I., Benyahia, M., Geczi, E., Kruck, U., Kosior, F., Masschelein, P., Candolfi, C., Dauscher, A., Koenig, J.D., Jacquot, A., Caillat, T., Alleno, E., Lenoir, B., 2021. High Power Density Thermoelectric Generators with Skutterudites. *Advanced Energy Materials* 11, 2100580.
- [51] Blandre, E., 2016. Thermal radiation at the nanoscale: near-field and interference effects in few-layer structures and on the electrical performances. Ph.D. thesis. Université de Lyon.